J Mater Sci (2009) 44:4429–4442
DOI 10.1007/s10853-009-3671-9

Microstructural studies of self-supported (1.5–10 μm) Pd/23 wt%Ag hydrogen separation membranes subjected to different heat treatments

W. M. Tucho · H. J. Venvik · J. C. Walmsley · M. Stange · A. Ramachandran · R. H. Mathiesen · A. Borg · R. Bredesen · R. Holmestad

Received: 12 March 2009 / Accepted: 6 June 2009 / Published online: 23 June 2009

Abstract The microstructure of self-supported 1.5–10-μm thick Pd/23 wt%Ag membranes grown by magnetron sputtering have been studied after heat treatment and hydrogen permeation tests using electron microscopy and synchrotron X-ray diffraction. After hydrogen flux stabilization and permeance measurements at 300 °C, the membranes were annealed in air at 300 °C or in N_2/Ar at 300/400/450 °C for 4 days and then tested for hydrogen permeation. The permeation results show that changes in permeability depend on the treatment atmosphere and temperature, as well as membrane thickness. Air treatment at ~300 °C generally induced a positive effect on permeation in the thickness range of 1.5–10 μm. Significant microstructural changes, including grain growth, strain relief, void formation, and growth of nodules occurred in the membranes. The changes in microstructure are more severe for the thinner membranes, and may be attributed mainly to the oxidation processes at or near the surface. For samples annealed in N_2/Ar, enhanced permeation was only obtained with treatment at ~450 °C for 5 and 10 μm. The changes in the microstructure generally increased with heat-treatment temperature, and decreased with membrane's thickness. The membrane with enhanced permeation was accompanied by significant grain growth, strain relief, and surface roughening. For all the membranes, the relative changes in the microstructure were substantially more prominent on the permeate surface than on the feed surface. Details of the analysis are presented and discussed.

W. M. Tucho · J. C. Walmsley · A. Ramachandran · R. H. Mathiesen · A. Borg · R. Holmestad (✉)
Department of Physics, NTNU, 7491 Trondheim, Norway
e-mail: randi.holmestad@phys.ntnu.no

H. J. Venvik
Department of Chemical Engineering, NTNU, 7491 Trondheim, Norway

J. C. Walmsley · M. Stange · R. Bredesen
SINTEF Materials & Chemistry, P.O. Box 124, Blindern, Oslo 0314, Norway

Introduction

The important role of advanced materials in a sustainable development is unquestionable. Technologies enabling production, handling, and use of hydrogen as an energy carrier are promising approaches for reducing green house gas emissions [1, 2]. Palladium (Pd)-based membrane technology has the capacity of producing high purity hydrogen from gas mixtures [3], e.g., for use in proton exchange membrane fuel cells. In particular, palladium–silver (Pd/23 wt%Ag) alloy thin films have been studied widely for hydrogen separation systems since they offer advantages over pure palladium in terms of higher permeability, higher resistance to embrittlement, and lower material cost. So far, most studies on Pd-based membranes have focused on hydrogen permeation properties. However, as pointed out by McLeod et al. [4], the reported hydrogen permeabilities differ nearly by an order of magnitude for Pd and Pd/Ag membranes in the 1-μm thickness approximately. The reasons for such scattered experimental results are most likely due to the differences in microstructure or impurities present at the surface and/or in the bulk of the membranes [4, 5]. Membranes with similar composition and thickness, but prepared by different

techniques, may consequently be expected to yield varying permeability characteristics.

Relatively few studies have reported correlations between microstructure, in particular grain size, and the permeation characteristics of Pd-based membranes [4–8]. Motivated by results from a theoretical model [9], Yao and Cahoon [7] studied grain boundary diffusion of hydrogen in polycrystalline nickel at room temperature using an electrochemical permeation technique. They compared permeation through fine and coarse-grained samples in the thickness range of 10–150 μm. Bulk diffusion was identified as the dominant process for hydrogen transport through the nickel films. Other groups reported higher hydrogen permeation through fine-grained Pd-based membranes than through a coarse-grained ones [8, 10]. According to these reports, hydrogen diffusion through grain boundaries is faster than through the grain interior. By contrast, grain boundaries, and particularly dislocations at the boundary junctions, have been suggested to act as weak trapping sites that retard hydrogen transport [11]. Other studies [6, 12, 13] also reported increased hydrogen permeation through Pd/Ag membranes with increased grain size after heat treatment. McLeod et al. [4] explained the relationship between permeation and grain size in Pd/Ag membranes in terms of the volume fraction of grain boundaries. A higher volume fraction of grain boundaries (fine-grained membranes) retards hydrogen diffusion as compared to that of the coarse-grained structures, where bulk diffusion dominates. According to Okazaki et al. [13], on the other hand, the enhanced permeation is mainly attributed to the structural rearrangement of Pd membranes that effectively reduces the inter-crystalline voids between large grain boundaries observed before grain growth. Xomeritakis and Lin [14] also observed higher permeation through coarse-grained rather than through fine-grained Pd/Al_2O_3 composite membranes.

In summary, the relation between microstructure and hydrogen diffusion in Pd-based membranes remains unclear. In view of this, this study aims to investigate and understand changes in the microstructure of sputtered, thin (1.5–10 μm), self-supported Pd/23 wt%Ag membranes annealed in air or N_2/Ar and subsequently subjected to hydrogen permeation tests. In particular, the objectives have been (i) to characterize the microstructure of the membranes using X-ray diffraction and electron microscopy techniques, (ii) to determine changes that might occur in the microstructure relative to the as-grown films, and (iii) to analyze whether the observed microstructure would show any trend with respect to the permeation properties. The permeation results of the membranes studied in this article are mainly reported in Ref. [12] and partly in Ref. [15].

Experimental

Material

A set of self-supported magnetron sputtered Pd/23 wt%Ag membranes [16], with thicknesses between 1.5 and 10 μm were prepared for this study. The different samples investigated are summarized in Table 1. In column 1, the sample designation numbers 1.5, 2.2, 5, and 10 refer to the nominal thicknesses 1.5, 2.2, 5, and 10 μm, respectively. "M" stands for membranes heat treated and subjected to hydrogen permeation tests, "AG" means as-grown film, and "a," "o," and "i" denote "air," "oxygen," and "inert" (N_2/Ar) gas exposure during heat treatment, respectively. The last three digits of the sample designation code provide the heat treatment temperature (in °C). For all the permeation experiments, the original growth surface formed during magnetron sputtering was kept facing toward the feed gas flow and is designated as the "feed surface." Consistently, the low pressure side of the membrane, labeled "permeate surface," corresponded to the surface facing the Si-substrate during sputtering. The membrane 2Mo300 was annealed in oxygen for 4 days, but not subsequently tested for hydrogen permeation.

Each membrane was initially ramped from room temperature to 300 °C at a rate of 4 °C min^{-1} in a furnace, with N_2 flowing on the feed side and Ar on the permeate side. This procedure was followed by stabilization for 1 day in a 1:1 H_2:N_2 mixture at a total flow of 200 NmL/min at the feed side and 50 NmL/min Ar sweep gas on the

Table 1 Overview of Pd/23 wt%Ag alloy membrane samples investigated with reference to permeation investigations

Membrane	Heat treatment		References
	Gas	T (°C)	
1.5Ma300	Air	300	[15]
2.2Ma300	Air	300	[15]
5Ma300	Air	300	[12]
10Ma300	Air	300	[12]
2MO300	O_2	300	
1.5Mi300	N_2/Ar	300	[15]
5Mi300	N_2/Ar	300	[12]
10Mi300	N_2/Ar	300	[12]
1.5Mi400	N_2/Ar	400	[15]
5Mi400	N_2/Ar	400	[12]
10Mi400	N_2/Ar	400	[12]
5Mi450	N_2/Ar	450	[12]
10Mi450	N_2/Ar	450	[12]
1.5AG	1.5 μm as-grown		
5AG	5 μm as-grown		
10AG	10 μm as-grown		

permeate side. After stabilization, the permeating H_2 flow was measured for a feed side flow of 200 NmL/min pure H_2 at 300 °C and without sweep gas being applied. The flux measured at this stage was used as reference for evaluating the performance of the membranes after heat treatment.

The membranes were then thermally treated for about 4 days in air at 300 °C or in N_2 (feed side) and Ar (permeate side) at 300, 400, or 450 °C. For heat treatment in air, the system was first flushed with N_2/Ar right after the flow stabilization and initial permeation measurement, and then equal flows of air were introduced on both sides of the membrane. After heat treatment, the permeating hydrogen flow was measured at 300 °C with differential pressures up to 43 kPa for the 5-μm and 53 kPa for the 10-μm thick membranes following the same procedure as above. The maximum differential pressure applied is well below the bursting pressures of the foils (e.g., ~80 kPa for a thickness of 1.5 μm) [15], minimizing plastic deformation as a result of the mechanical stress provided by the applied pressure difference. At the end of the tests, the membranes were cooled down to a room temperature at a rate of 4 °C min^{-1} in N_2/Ar. A more detailed description of the heat treatment and permeation procedures is reported elsewhere [12, 15].

X-ray diffraction and electron microscopy

The high-resolution powder diffractometer of the Swiss-Norwegian Beamlines (SNBL) at the European Synchrotron Radiation Facility (ESRF) in Grenoble, France, was used for X-ray diffraction (XRD) experiments. Details on the beam line and its instrumentation are given elsewhere [17]. The X-ray diffraction experiments were performed in a near-grazing-incidence reflection geometry to provide a convenient orientation for measurements of all the low index peaks, given the strong ⟨111⟩ type preferred orientation parallel to the surface normal in all the samples. Since the measured X-ray peak profiles are a convolution of the sample characteristics and the instrument resolution function, the latter must be sufficient to resolve the intrinsic sample characteristics that can be related to peak broadening effects, such as finite grain sizes and residual strains [18]. The intrinsic instrument angular resolution with incident X-rays monochromatized to 15.566 keV was roughly $\Delta 2\theta \sim 0.005°$.

Extraction of strain and crystal size was based on a profile fitting by Rietveld refinement of a multiple-peak diffraction pattern [19]. In this study, the special sample orientation provided complete diffraction patterns to $2\theta \sim 44°$, where all the five low index peaks had a signal-to-noise ratio well above the background. The profile fitting and analysis was performed using the General Structure Analysis System (GSAS) program [20] employing established procedures for strain- and size-broadening analysis [21]. A Pseudo-Voigt function was used for the peak shape profile fitting [19, 21]. In addition to the profile parameters, the refinement included the face centered cubic (fcc) lattice parameter, 3–5 background coefficients, an isotropic atomic displacement parameter, a 2-parameter model to compensate for preferred orientation effects, and, a scale factor. Grain size, D_v, and the average elastic strain of the diffracting grains ε, can be estimated from the profile parameters refined in GSAS employing expressions for isotropic strain and size-broadening suggested by Karen and Woodward [22]. Refined parameters from a Si standard were used to account for the instrumental broadening.

Transmission Electron Microscopy (TEM) investigations were performed using a Philips CM30 operating at 200 kV. High Resolution (HR) TEM and Scanning Transmission Electron Microscopy (STEM) composition analyses were performed using a JEOL 2010F operating at 200 kV, equipped with an Oxford Instruments Energy Dispersion Spectroscopy (EDS) detector. Samples were investigated both in plan-view and cross-section geometry, prepared according to procedures established previously [23]. Grain size measurements were performed as described in the same report [23]. The lateral grain size was measured directly from bright and/or dark field TEM images. The grains were selected from about 100–200 nm below the membrane surfaces for all the samples. The procedure used is based on the random intercept by grain boundaries of a test line parallel to the membrane surface. The grain size is then, $D_L = L/N_L$, where N_L is the number of intercepts with grain boundaries and L is the total length of the intercept line [24]. The mean values calculated were measured from about 200 grains in each sample. A field-emission Scanning Electron Microscope (SEM), Hitachi s-43000se, was used to study morphology and composition of the surfaces.

Results

Hydrogen permeation

The hydrogen flux through Pd-based membranes is generally expressed according to Fick's first law [25],

$$J = \frac{Q}{l}\left(P_1^n - P_2^n\right) \quad (1)$$

where J is the hydrogen flux in mol/(m^2 s), Q is the permeability in mol·m/(m^2 s Pa^n) and l is the membrane thickness in m. P_1 and P_2 are the hydrogen partial pressures (Pa) on the feed and permeate sides of the membrane, respectively, and n is the hydrogen pressure exponent. The

ratio Q/l is referred to as hydrogen permeance or pressure normalized flux. In principle, n approaches 0.5 if Q is independent of pressure, then bulk diffusion is rate controlling step or 1 if surface processes such as adsorption and desorption limit the transport [26–28]. n-Values between 0.5 and 1 are often found experimentally; however, the pressure range applied here is insufficient for unique determination of n [29].

The hydrogen permeance and permeability values using $n = 0.5$ are given in Table 2. The experiments and the underlying data are presented and discussed in more detail elsewhere [12, 15]. Before heat treatment, samples within the same thickness category are expected to have identical permeability, but Table 2 reveals some variations that may be attributed to slight differences in microstructure and/or experimental procedures. We have measured an average thickness of 6.1 ± 0.4 μm from TEM images and permeance of (4.3 ± 0.3) 10^{-3} mol/(m^2 s Pa$^{0.5}$) for the 5-μm samples. The corresponding values for the 10-μm samples are 11 ± 1 μm and (2.4 ± 0.3) × 10^{-3} mol/(m^2 s Pa$^{0.5}$), respectively.

Heat treatment in air at 300 °C increased the hydrogen permeability by approximately 15%, while the heat treatment in N_2/Ar at 300 and 400 °C led to a reduced permeability for the 5 and 10-μm membranes, as shown in Table 2. After heat treatment at 450 °C in N_2/Ar, the permeability was significantly enhanced for the 5-μm sample (5Mi450) but slightly reduced for the 10-μm membrane (10Mi450). The selectivity of the membranes was close to 100% before and after the treatments as assessed by experiments using He gas.

Grain size and micro-strain

Average grain sizes and strains estimated from the XRD profile analysis and size measurements from TEM micrographs for a series of 10-μm membranes are given in Table 3. Some deviations between the XRD and TEM measured grain sizes, in particular for the substrate/permeate side are seen. The discrepancies can partly be explained in terms of the differences in the probing volume between the two techniques. The grain sizes measured from TEM micrographs were obtained according to the procedures described in "X-ray diffraction and electron microscopy" section, where the complete probing volume extends roughly 0.2 μm inward from the surface. In the particular geometry chosen for the XRD experiment, the monochromatized incident beam at 15.566 keV directed at a low incident angle, give a full X-ray penetration depth of ~2.8 μm (at a 1% signal cutoff). Since X-ray diffraction signals from the deeper parts of the volume will be severely weakened by X-ray absorption, due to a long total beam path inside the sample, the near-surface grain contributions

Table 2 H_2 permeance (mol/(m^2 s Pa$^{0.5}$)) and permeability (mol/(m s Pa$^{0.5}$)) of the 5 and 10 μm of Pd/Ag membranes before and after heat treatment as measured at 300 °C

Sample	Thickness (μm)	Before heat treatment		After heat treatment		Percentage difference (%)
		Permeance ($\times 10^{-3}$)	Permeability ($\times 10^{-8}$)	Permeance ($\times 10^{-3}$)	Permeability ($\times 10^{-8}$)	
5Mi300	6.0	4.58	2.75	3.07	1.84	−33
5Mi400	6.5	4.40	2.86	3.11	2.02	−29
5Mi450	5.5	3.89	2.14	5.12	2.82	+32
5Ma300	6.3	4.38	2.76	5.07	3.19	+16
10Mi300	10.0	2.06	2.06	0.73	0.74	−64
10Mi400	11.7	2.46	2.88	1.60	1.88	−35
10Mi450	9.8	2.38	2.33	2.23	2.17	−7
10Ma300	11.4	2.70	3.08	3.11	3.54	+15

Table 3 Measured thickness, grain size, and micro-strain for the 10-μm Pd/Ag membrane samples as estimated by XRD and TEM

Sample	Grain size (nm) TEM		Grain size (nm) XRD		Micro-strains ε ($\times 10^{-4}$) XRD	
	Growth/feed	Substrate/permeate	Growth/feed	Substrate/permeate	Growth/feed	Substrate/permeate
10AG	100	12	84	41	20.7	23.6
10Mi300	92	28	83	44	17.8	12
10Mi400	84	40	94	58	17.0	8.2
10Mi450	88	64	109	115	9.9	10.3
10Ma300	98	49	82	83	12.7	8.7

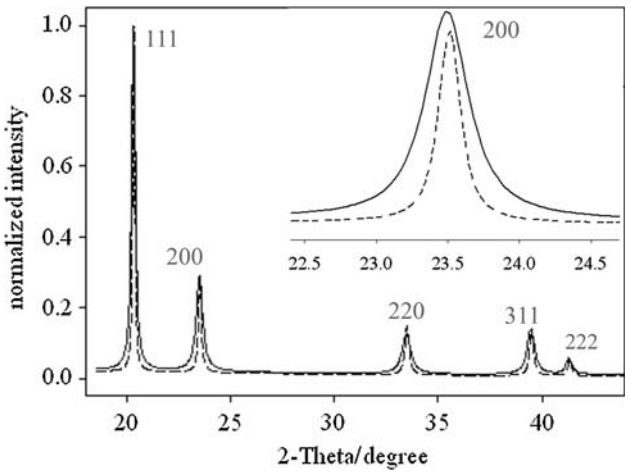

Fig. 1 XRD diffractograms from the substrate/permeate side of as-grown (10AG, *solid lines*) and a heat-treated membrane in N_2/Ar at 400 °C (10Mi400, *dashed lines*). The inset compares the line widths of the (200) reflection

dominate the total peak intensity profiles. Accordingly, the mean penetration depth for the XRD measurements was roughly 0.6 μm.

Examples of XRD patterns for 10Mi400 and 10AG are shown in Fig. 1. The inset shows details of the (200) peaks. The line widths for the heat-treated sample are narrower than for the as-grown one, indicating both grain growth and strain relaxation. The latter can be confirmed by comparing 10Mi400 and 10AG lattice parameters, $a_{10\text{Mi}400} = 3.9242(3)$ Å and $a_{10\text{AG}} = 3.9273(3)$ Å, where the elastic part of the strain relaxation from heat treatment can be assessed directly, as $\Delta a/a_{10\text{AG}} = 7.8 \times 10^{-4}$. Similarly, the strain relaxed in 10Ma300 is about 5.3×10^{-4}.

The TEM-based estimates show that the grain size near the growth surfaces is larger than at the substrate interfaces by about 4 and 8 times, for the as-grown samples, 5AG and 10AG, respectively. During heat treatment, grains on the growth/feed surfaces of 10Mi300 and 10Mi400 are nearly unchanged, whereas the grain size on the substrate/permeate side increased significantly. The 5-μm membranes show similar trends to the 10-μm membranes with respect to grain growth. After treatment at 450 °C, grains close to the substrate/permeate surface have attained similar size as those close to the growth/feed surface. The grain growth in the air-treated membranes also seems predominant at the substrate/permeate surfaces.

The average strains measured for the tested membranes are consistently lower than for the as-grown films, indicating stress release during heat treatment. Such strain relaxation remains fairly constant, but was found to be slightly higher at higher treatment temperatures. The relaxations are consistently higher on the substrate/permeate side where the coarsening effect is also high.

Microstructural analysis by TEM and SEM

Elevated temperature treatment of thin Pd/Ag films is known to alter both the bulk microstructure and surface morphology [15, 30]. Figure 2 shows SEM micrographs of the 10-μm membranes illustrating the development of surface topography with treatment temperature and atmosphere.

The topographic changes of the growth/feed surfaces in 10Mi300 (c) and 10Mi400 (e) are relatively modest, relative to 10AG (a), where the surface roughness appears to be similar. In contrast, growth/feed surfaces of 10Mi450 (g) and 10Ma300 (i) developed significant roughness, in addition to pitting in 10Ma300. The substrate/permeate surfaces all developed significant roughness, as shown in Fig. 2d, f, h, j relative to the substrate interface of the as-grown film (b). The roughness at the substrate/permeate surface evolved with N_2/Ar annealing temperature, although it is most severe after exposure to oxidizing environments and subsequent reduction during hydrogen permeation. The relative changes in surface roughening and grain morphology observed by SEM and TEM correlate well with the grain coarsening and strain relaxation presented in Table 3.

The 5-μm membranes undergo topographical changes similar to those found for the 10-μm membranes. Figure 3 display bright field TEM cross-sectional micrographs showing the growth/feed (a–d) and substrate/permeate (e–h) surfaces, respectively, for the 5-μm membranes. Whereas Fig. 4 shows pits developed on the feed surface of 5Mi450 in cross-section geometry. Apparently, the relative changes in the surface topography and microstructure are larger for the substrate/permeate surfaces than for the growth/feed surfaces (Fig. 3).

Voids with relatively small sizes were observed close to the substrate/permeate surfaces of 5Mi400 and 5Mi450, as shown in Fig. 3g, h, respectively. Most of these voids developed at grain boundaries and triple junctions. Figure 5a shows voids near the substrate/permeate surface of 5Mi450 and Fig. 5b displays a magnification of the region indicated in (a). Examples of voids formed at the grain boundaries are marked as "g" and at the triple junctions as "T" in Fig. 5b. Some tiny voids observed in the grain interior.

The air-treated membranes developed structural changes, which were more pronounced in the thinner membranes. Figure 6 displays full-thickness bright field TEM micrographs of the as-grown film, 1.5AG (a), and a tested membrane, 1.5Ma300 (b). Significant void formation and surface roughening were evident after thermal treatment in air. Some of the voids appear as holes, since their size exceeds the thickness of the TEM sample (the electron transparent region is ca. 60 nm thick for this material). The

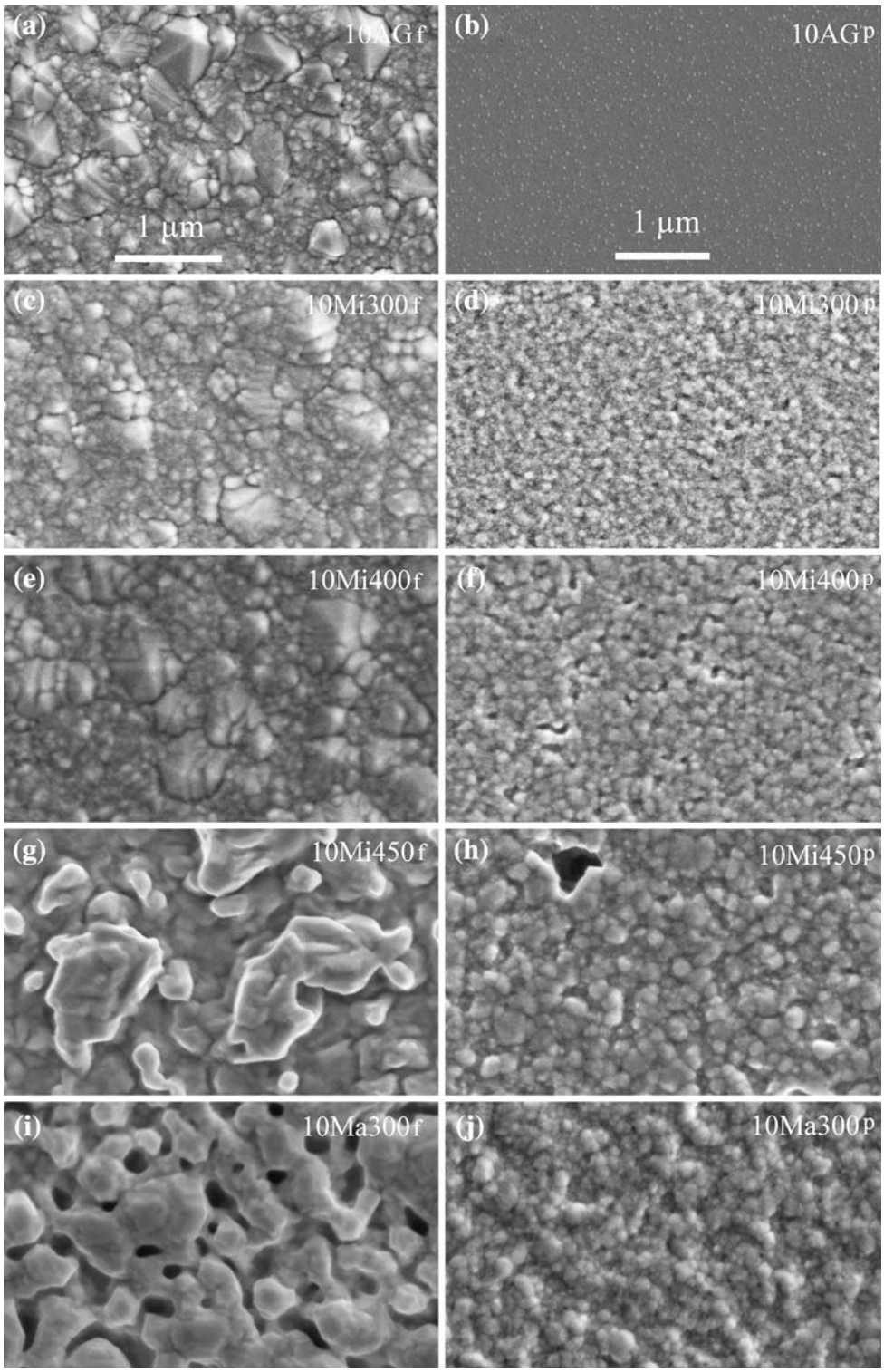

Fig. 2 SEM micrographs comparing the surface topography and grain morphology of the 10-μm membranes. The images on the left side represent growth/feed and on the right represents substrate/permeate surfaces. All the images have the same magnification with scale bars shown in (**a**) and (**b**) only. **a**, **b** As-grown (10AG—reference); **c**, **d** 10Mi300; **e**, **f** 10Mi400; **g**, **h** 10Mi450 and **i**, **j** 10Ma300. The suffixes "f" and "p" to the sample codes stand for feed and permeate, respectively

largest voids were formed in the region near the substrate/permeate surface. The voids formed near the substrate/permeate region were generally larger than those near the growth/feed surface.

Some of the voids in the 1.5Ma300 near the substrate/permeate surface are as big as 200 nm, and others turned into pits where they outcrop the surface. This is shown in Fig. 7b, where the finer details of the surface and smaller voids also can be seen. These voids were generally formed at approximately equal depths below the surfaces. They were also more severe for thinner membranes than the thicker ones. Crystals neighboring some of the bigger voids

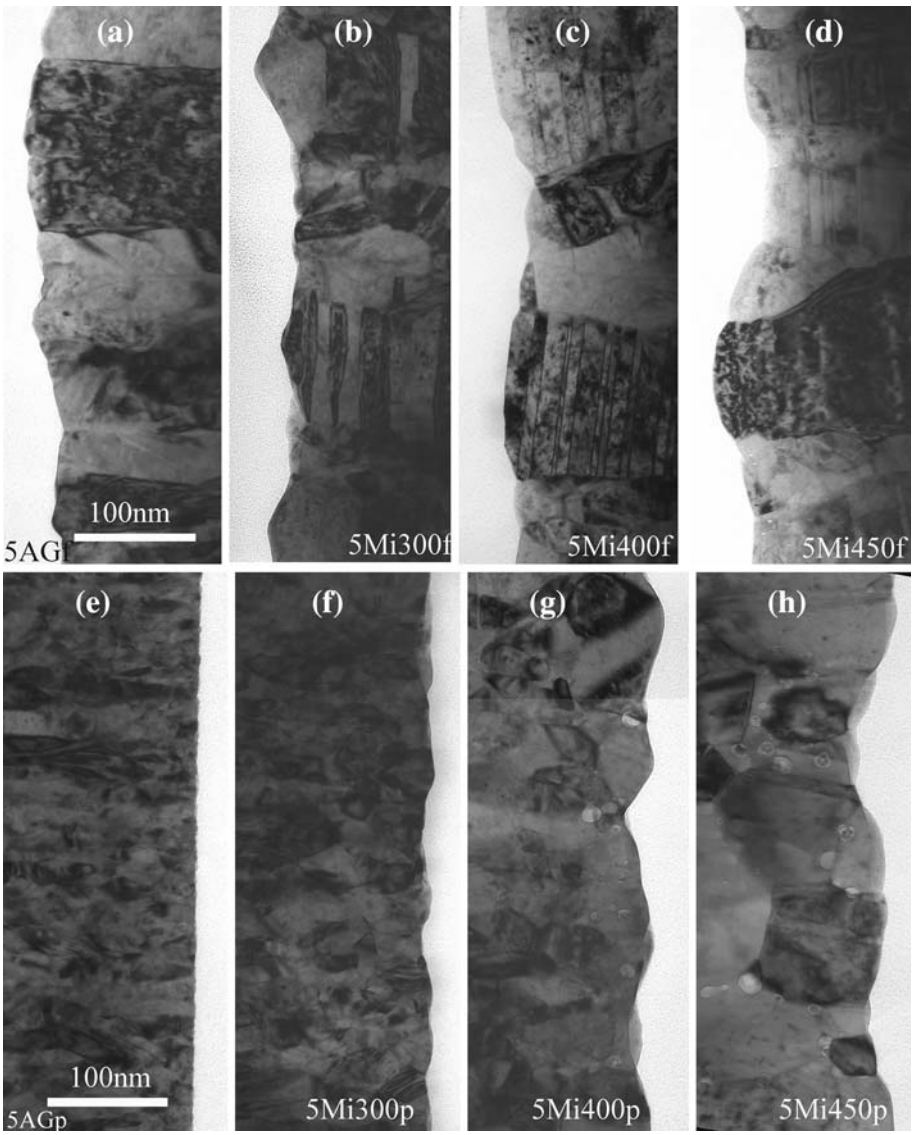

Fig. 3 TEM cross-section images of growth/feed (*left*) sides (**a**–**d**) and substrate/permeate (*right*) sides (**e**–**f**) of 5AG (**a** and **e**), 5Mi300 (**b** and **f**), 5Mi400 (**c** and **g**) and 5Mi450 (**d** and **h**). Voids are seen in (**g**) and (**h**). All the images have equal magnification with the scale bars as shown in (**a**) and (**e**). The suffixes "f" and "p" to the sample codes stand for feed and permeate, respectively

appear to be reoriented. The {111} twin planes of the twin lamellae near the growth surface of the as-grown films usually are oriented parallel to the surface [23], but in Fig. 7a, they were reoriented nearly normal to the surface.

Figure 8 shows the growth/feed surface of 5Ma300 in TEM cross-section (a) and plan-view SEM image (b). The voids shown in (a) are located about 50 nm below the feed surface. Dark spots in (b) are pits of varying size, up to 50 nm. There are no pits and big voids observed near the substrate/permeate surface, rather nodules of various sizes as described below.

As shown in Fig. 7, some of the voids appear to contain amorphous material. A higher magnification image from 2.2Ma300 with similar voids is shown in Fig. 9. The material inside the void is amorphous, but from EDS analysis there is no indication of oxide or other elements different from Pd and Ag in the amorphous area. The contrast difference shown is therefore attributed to local variations in thickness.

In order to further understand the factors related to void formation, we have analyzed and compared the chemistry, microstructure, and surface morphology of a 1.5-μm thick sample 2Mo300, annealed at 300 °C in oxygen for 4 days, but not subsequently exposed to hydrogen permeation. The analysis of this sample can give information about the oxide layer formed during heat treatment in oxygen atmosphere. STEM/EDS spectra from the surface and near surface region of the 2Mo300 sample show oxygen, and measurement by XPS also confirmed presence of oxide phase [31]. Similar EDS spectra from 1.5Ma300, 5Ma300, and 10Ma300 did not show any peak for oxygen.

TEM cross-sectional images of 2Mo300 are shown in Fig. 10 (TEM-measured thickness is 2 μm). A high number of small voids were formed close to both the feed/

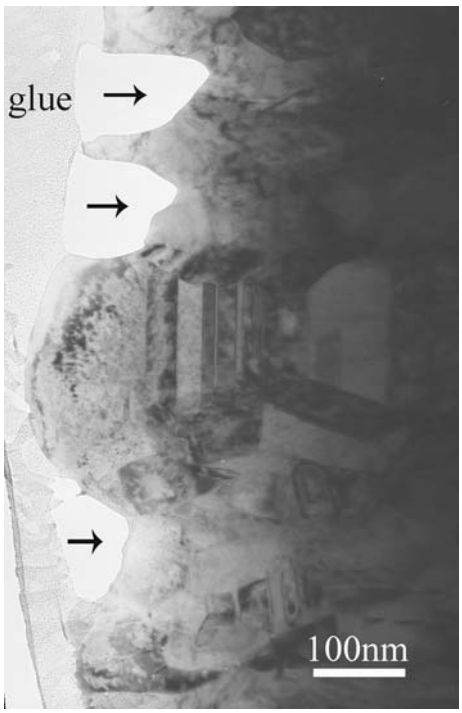

Fig. 4 TEM cross-sectional image showing pits (indicated by *arrows*) on the growth/feed side of the 5Mi450 membrane

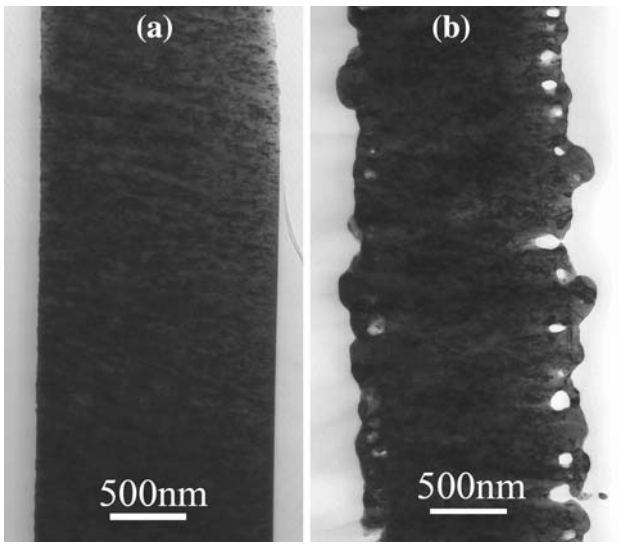

Fig. 6 TEM full thickness image of 1.5-μm membranes in cross-section geometry: **a** as-grown (1.5AG), **b** after 300 °C heat treatment in air and subsequent 300 °C hydrogen permeation measurements (1.5Ma300). Growth/feed surfaces face left and substrate/permeate surfaces face right

growth and permeate/substrate surfaces as shown in (a) and (c), respectively. Full-thickness image of 2Mo300 is shown in Fig. 10b.

For some air-treated samples, protruding grains or nodules developed, as illustrated at the permeate surface of 5Ma300 shown in Fig. 11 for both cross-section TEM and plan-view geometry in SEM. Similar nodules were also formed at the substrate/permeate surface of 2.2Ma300. The nodules are evenly distributed across the surface, are ~90 nm in diameter, and extend up to 100 nm out of the surface. Each of these nodules increased the local surface area by ~300%, assuming cylindrical grains ending in a hemispherical shape at the top. This indicates that the total surface area of the permeate surface could be increased by about 10% by the formation of such nodular grains. Contrary to 5Ma300, nodules were not formed in 10Ma300. In this sample, only tiny and very few voids close to the permeate surface developed.

STEM/EDS compositional mapping revealed similar compositions of the nodules as that of the underlying bulk. The dark-field image in Fig. 12 illustrates that the nodules are merely one single grain and have grown from an already existing grain in the membrane. The inset is a selected area electron diffraction pattern. The reflection from which the dark field image of the nodule is selected corresponds to the (220) reflection.

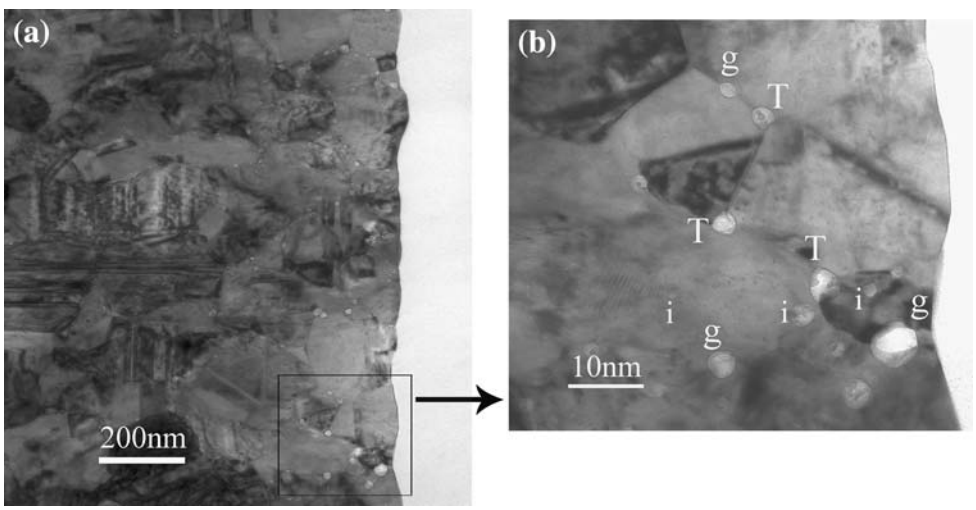

Fig. 5 TEM images showing voids near the substrate/permeate surface after N_2/Ar 450 °C heat treatment and subsequent 300 °C permeation measurement of the 5-μm membrane (5Mi450). **a** Low magnification image with many voids of different sizes, mainly located in the grain boundaries and at triple junctions. **b** Details of the region marked in (**a**). Voids at triple junctions and grain boundaries are labeled "T" and "g," respectively, and "i" for the voids in the grain interior

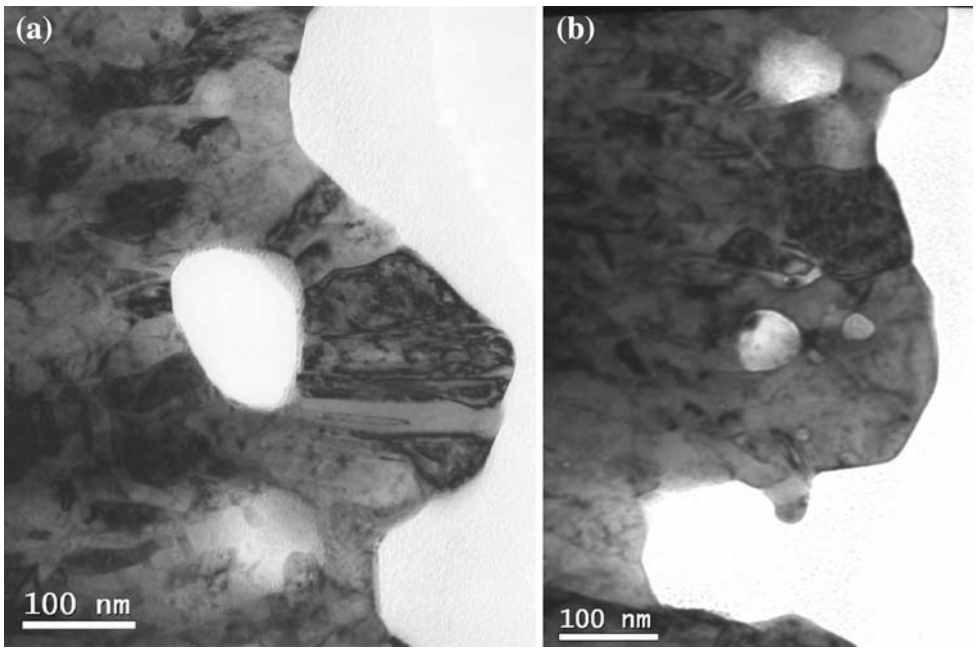

Fig. 7 Magnified TEM image of growth/permeate near the surface region of the 1.5-μm membrane after heat treatment in air at 300 °C and subsequent 300 °C permeation measurement (1.5Ma300). **a** Large, ~150 nm void accompanied by re-orientation of crystallographic planes. **b** Typical pit (~200 nm deep) and voids of different size

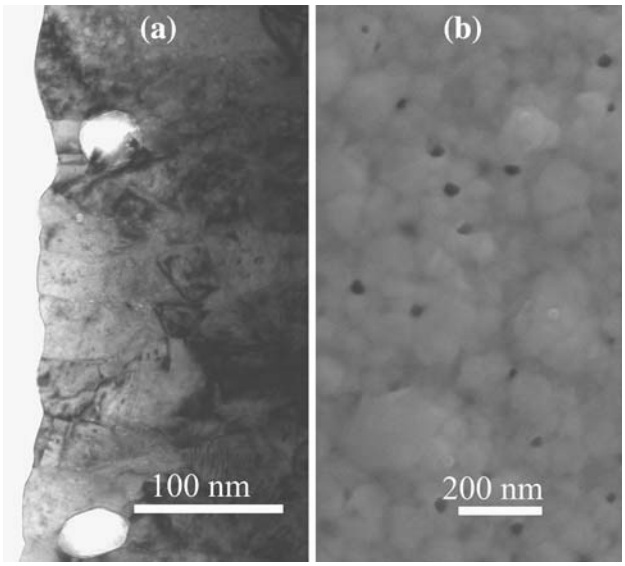

Fig. 8 Growth/feed side of 5-μm membrane after heat treatment in air at 300 °C and subsequent 300 °C permeation measurements (5Ma300). **a** TEM bright-field image showing voids of various magnitudes in the near-surface region. **b** SEM image showing surface features, pits appearing as dark spots

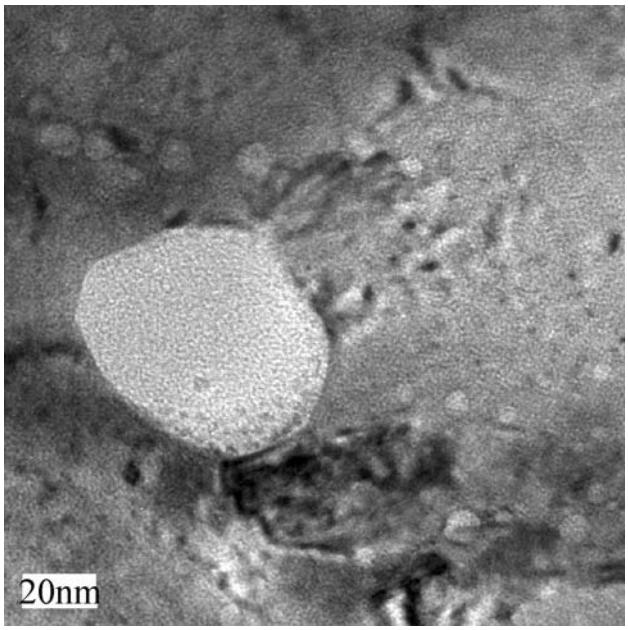

Fig. 9 High-resolution TEM images of a void near the growth/feed surface of the 2.2-μm membrane after heat treatment in air at 300 °C and subsequent 300 °C permeation measurement (2.2Ma300). A large void surrounded by tiny voids

Discussion

This and previous studies [15, 23] confirm that the as-grown, freestanding Pd/Ag films prepared by magnetron sputtering are free of mechanical flaws, such as micro-cracks, pinholes, inter-granular porosity, and cavities. The as-grown films are characterized by tiny crystallites and a high density of lattice defects, including stacking faults, triple junctions, and dislocations at and close to the substrate surface. At the growth surface, the grains attain a columnar structure aligned parallel to the growth direction, and laterally the grain size is rather homogeneous. The lateral grain size decreases toward the substrate-interface surface, where the grains are non-columnar, fine sized (~5–20 nm), and display a non-preferential orientation. The substrate–interface surface is very smooth, whereas the growth surface is rougher. Lateral grain size and surface

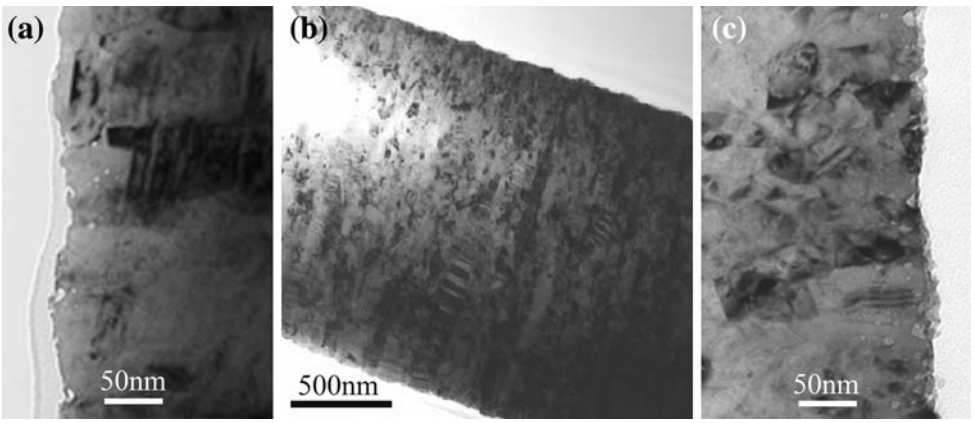

Fig. 10 TEM cross-sectional images of a 2-μm membrane after heat treatment in oxygen at 300 °C and not subsequently tested for hydrogen permeation (2Mo300). **a** Growth/feed surface (*left*). **b** Full-thickness (*feed surface is bottom edge*). **c** Substrate/permeate surface (*right*). Voids of a few nanometers in size are seen close to both feed and permeate surfaces

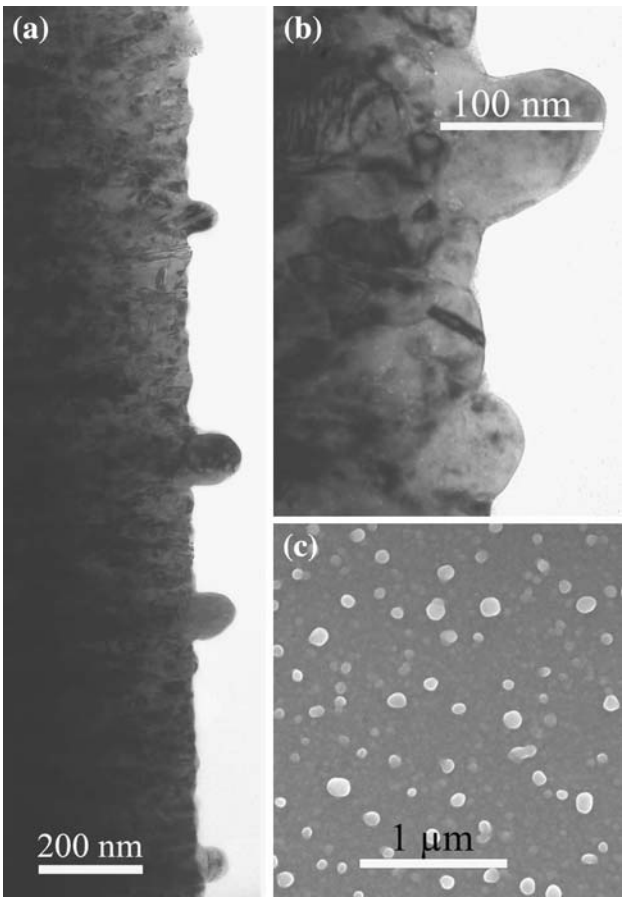

Fig. 11 Nodules (protruded grains) developed at the substrate/permeate surface of the 5-μm membrane after heat treatment in air at 300 °C and subsequent permeation measurements (5Ma300). **a** Population of the nodules in cross-sectional TEM image. **b** Magnified TEM image of a nodule. **c** SEM image in plan-view showing the population of the nodules

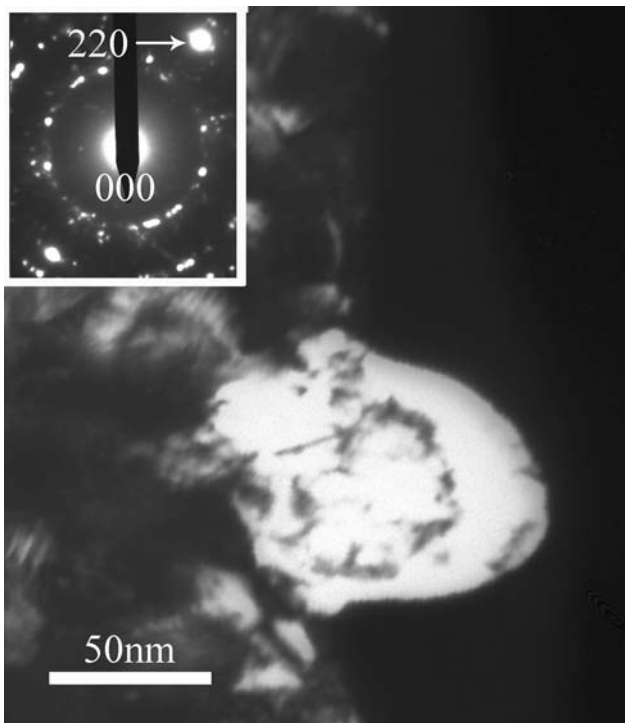

Fig. 12 TEM cross-sectional dark-field image from a (220) reflection of a single nodule at the substrate/permeate surface of the 5-μm membrane after heat treatment in air at 300 °C and subsequent 300 °C permeation measurement (5Ma300), suggesting the nodule is a single grain. The inset image shows a selected area diffraction pattern with (220) reflection spot labeled

roughness at the growth side generally tend to increase with increasing thickness of the films.

The microstructure of the Pd/Ag films/membranes is expected to change upon annealing and/or hydrogen permeation. These changes can be analyzed in two stages: after permeation stabilization, and after heat treatment and permeation. The changes in microstructure that could occur during permeation stabilization under large H_2 concentration gradient across the membranes can not be excluded. For example, Shu et al. [32] observed Pd and Ag enrichments on the high and low pressure sides, respectively, after exposing Pd/25 wt%Ag samples to hydrogen permeation. Such changes are believed to be the same since similar conditions were applied to all the membranes in this study as described in "Material" section. In addition, the

microstructural changes that occurred during the permeation stabilization are relatively less significant compared to the changes developed due to heat treatment atmospheres and temperatures. Therefore, the following sections discuss mainly the relative differences observed in the microstructure of the membranes that are believed to occur after heat treatment and/or permeation experiments.

Microstructures of the annealed and tested membranes

The driving force for individual grain growth processes in a polycrystal can be expressed by a Gibbs-Thompson (GT) relation of the kind, $\Delta\mu = 2\gamma V_a/d$, where V_a and d are the atomic volume and size of the grain, respectively. The second rank tensor, γ expresses the local grain boundary tension in the polycrystal, which depends both on the grain boundary energy and final gradients in strain rates between the neighboring grains, and $\Delta\mu$ is the chemical potential [33]. In the absence of strain, the grain growth process corresponds to a classical Ostwald ripening. According to the GT relation, grain growth is expected to be more pronounced at the permeate surface on heating, due to its higher density of grain boundaries (smaller grains) providing more excess-free grain boundary energy and consequentially, a larger driving force for grain growth [34, 35]. Grain boundary energy may be affected by the added solute segregating to the grain boundary [35], but evidence of such segregation was not found in the bulk. In general, oobservations from both XRD and TEM measurements (Table 3) agree well with the GT scheme, showing significantly higher grain growth at the permeate surface than at the feed surface. The final grain size is a function of the heat treatment temperature.

In this study, the trend in grain growth is apparent, as shown in Table 3. The grain sizes at the substrate/permeate side of the membranes heat treated in N_2/Ar increase with increasing temperature. After heat treatment at 450 °C, the grains at the substrate/permeate surface have attained about the same size as the grains on the growth/feed side of the film. The substrate/permeate surface is necessarily associated with lower activation barriers and lower onset temperatures for coarsening relative to the growth/feed surface, with a lower free excess energy. Heat treatment at intermediate temperatures activates fewer of the grains than at higher temperatures where more grains become activated. Our observations suggest that the temperature required for the initiation of substantial grain growth lies between 400 and 450 °C. Enhanced hydrogen flux was also observed at 450 °C [12]. The result is in agreement with reports in the literature. Remarkable grain growth was reported in a similar temperature range, for example, 400–500 °C for Pd/Ag membranes [36] and, at 420 °C for PdIn thin films [37]. Surface roughening is also known to occur in relation to the coarsening processes, accounted for by the same driving forces as the grain growth [38, 39].

Strain in the as-grown films can be due to lattice defects such as dislocations, and can be relaxed by diffusion of matter between the bulk of the film and its surface. Furthermore, in thin films, stress relaxation can generate plastic deformation followed by other defects, such as microcracks and voids [40].

The voids observed in the membranes annealed in N_2/Ar at 400 and 450 °C may be related to local stress concentrations. In these membranes, the voids observed are mainly located in the grain boundaries and in the triple junctions (e.g., Fig. 5). These sites, especially triple junctions, may act as stress concentrators [41, 42]. Apparently, the voids could be formed during annealing through strain relaxation. The fact that such voids were not seen in the membranes heat treated in N_2/Ar at 300 °C suggests a certain critical temperature above which observable voids are formed. The void formation may also be initiated or expanded by hydrogen diffusion in the stress fields associated with structural defects, such as edge dislocations, grain boundaries, and triple junctions. The hydrogen atoms can diffuse into these defects and recombine to form H_2 [43, 44]. The pressure developed inside the voids, may, however, not likely exceed the external or the applied hydrogen partial pressure [43]. Furthermore, it is more likely that the voids were created during the 4 days of heat treatment at 400/450 °C in N_2/Ar rather than during hydrogen diffusion ($\sim$3–5 h at 300 °C).

As indicated in the TEM images shown, for example, in Fig. 6, the membranes which were first heat treated in air at 300 °C and then reduced in hydrogen developed larger voids within 200 nm of the surfaces. By contrast, the voids formed in the samples which were only annealed in oxygen and not reduced (2Mo300), were tiny (less than $\sim$10 nm in diameter), but higher in density and extended as far as 100 nm from both surfaces, as shown in Fig. 10. Chemical analysis by EDS shows that only 2Mo300 contains oxygen species at and/or near the surface region. Oxygen was not observed by EDS in/near the surface of Ma300. This has been also confirmed by Auger and XPS studies [31]. In addition, voids were not observed in the membranes heat treated in N_2/Ar (e.g., 5Mi300) at the same temperature as 5Ma300.

We tentatively suggest that the formation of larger voids arises from the oxidation–reduction process. The selective oxidation of Pd over Ag under oxygen/air leads to segregation between the two elements in the near-surface region and enrichment of Pd at the surface [31]. A PdO_x layer is formed at the surface [31] and diffusion of oxygen may occur along extended defects, such as the grain boundaries, beneath the surface. Oxygen permeation through Pd membranes is, however, very low even at much higher

temperatures as shown by Gegner et al. [45]. Some oxide formation, particularly along fast diffusion paths, such as grain boundaries, could perhaps occur. One may speculate whether the lattice distortion and volume expansion due to oxide formation and subsequent volume contraction upon reduction could lead to formation of the voids, similar to the ones shown in Fig. 10a, c. During hydrogen permeation measurements, further growth of the voids could occur (compare, for example, Figs. 6b and 10). Hydrogen may also react with oxygen in the voids to form H_2O species that can contribute to the growth of the voids, e.g., by pressure build-up. On the other hand, the voids observed in 2Mo300 may also be facilitated by the oxide layer at the surface.

The nodule formation seems to depend on grain size distribution and atmosphere. Nodules developed only in some membranes heat treated in air and on the substrate/permeate surface, where the grains are small and lattice defects are denser than in the growth/feed surface. Aggarwal et al. have also observed nodules at the surface of nanocrystalline 20–400 nm Pd-films heat treated in air, but not on epitaxially grown films [46]. According to the authors, the development of the nodules is based on the oxidation of palladium, accompanied by a volume change of 38% that introduced compressive stress. The nodule formation in this study could also be caused by similar mechanisms. The absence of nodules at the growth/feed surface might be due to the large grain size that provides less favorable conditions. This suggests that the formation of the nodules is facilitated by grain boundary diffusion. Furthermore, the nodules were most likely formed during heat treatment due to the mass transporting/restructuring involved and not during the hydrogen permeation. Impurities (if any) at the surface may have also contributions in the nodule formation process as a result of interaction with oxide layers. In the thinnest membrane (1.5Ma300), surface roughening and void formation seemingly dominate over the nodules. Voids were also not observed when nodules developed. Further systematic studies are, however, needed to elaborate factors governing nodule formation.

Membranes fabricated from different targets and different batches probably have some variation in their microstructures. This is supported by the fact that the initial hydrogen flux showed significant differences between membranes with similar thicknesses [12]. Furthermore, as shown from the references in Table 1 [12, 15], the membranes analyzed in this study were sputtered and tested under slightly different conditions and at different times (2 years apart). The 5 and 10-μm membranes were produced from the same target, whereas the 1.5 and 2.2-μm membranes were from another target. In addition, the growth parameters in one batch may vary slightly and make small variations through the film thickness. Due to limitations in the geometry of the sputtering apparatus, thickness variations in the films are also expected. Even though the reproducibility of the membrane fabrication is generally satisfactory in terms of permeability and versatility of the films, the abovementioned differences appear to influence the resulting microstructure that may induce variations in permeation.

Relationship between microstructure and hydrogen permeance

The average permeance values given in "Hydrogen permeation" indicate that the flux–thickness relationship predicted by Eq. 1 is satisfied. This implies that bulk diffusion is the rate-controlling mechanism for the membranes before heat treatment. After the different treatments, only one permeation measurement exists for each thickness and treatment. The picture is complex since enhanced or reduced permeation is obtained, depending on the atmosphere and the temperature. A relationship between permeance and thickness remains, however, indicating that the permeation is still partly controlled by transport processes in the bulk of the material.

Heat treatment in air at 300 °C is a well-established procedure for permeation enhancement of sputtered Pd/Ag membrane in the thickness range of 1–10 μm [12, 15]. The enhancement of permeation varied in the range 15–130%, but with less scattered permeance values and better compliance with the permeance–inverse thickness relation after the treatment [31]. In terms of microstructure, the membranes showed substantial surface modification, including roughening and formation of pits and nodules that increase the total surface area. As noted previously [15], increased total surface area increases the number of sites available for dissociation/association, thereby contributing to the enhancement of hydrogen permeation. There are instances where Pd enrichment still remains at the surfaces of the air-treated membranes even after hydrogen permeation measurements [31]. Similarly, there is also a case where higher Ag concentration was observed at the surface for the air-treated membrane than that of as-grown sample [31]. The reasons for this deviation are, however, not known and inconclusive from these studies.

Our studies [12, 31] strongly indicate that flux depends on the membrane thickness, so that surface kinetics is not evidently a rate-limiting process. The membranes have also shown significant grain growth and stress relief. This study further reveals that surface modification and changes in microstructure were more dominant for the thinner membranes than for the thicker ones. Correspondingly, the relative increase in flux is higher for the thinner membranes than the thicker ones [12, 15].

The reduced permeation obtained after heat treatment in N_2/Ar at 300 and 400 °C for the 5 and 10-μm membranes

was unexpected (see Table 2) [12]. Enhanced permeability after heat treatment in N_2/Ar at 400 °C for similarly prepared 1.5 and 2.2-μm Pd/Ag membranes has been reported elsewhere [15]. This suggests that the effect of heat treatment in N_2/Ar on the permeability may depend on both the heat treatment temperature and the membrane thickness. The 5 and 10-μm thick membranes showed significant grain growth and strain relaxation for the heat treatment in N_2/Ar at 450 °C and for which enhanced permeation was observed. At 400 °C and below, the membranes experienced smaller, but similar microstructural changes than the membranes, which demonstrated enhanced permeation. The reason for the reduced permeation is hence not fully understood from the microstructural analysis. The surface analysis indicated segregation of silver to the membrane surface upon N_2/Ar heat treatment [31], but given thickness dependency of the permeance, we believe that the permeation data cannot be fully explained without considering the changes in the bulk microstructure that affect the hydrogen transport properties. The bulk effects could be related to the observed surface segregation and/or undetected defects.

Lattice defects, such as dislocations and voids, are potential traps where the mean residence time of hydrogen could be longer than that in defect-free regions [47]. Hydrogen, at the internal free surfaces of the voids and cavities, can be adsorbed/desorbed as it does at the external surface [48] and then recombine to form H_2. In the voids, hydrogen is trapped temporarily, resulting in decreased apparent diffusivity with increasing hydrogen concentration and probably increased density of the voids [49]. This suggests that the net concentration of hydrogen in the bulk with voids is larger than without voids, leading to increased apparent solubility, but reduced diffusivity. Larger voids, as shown in 1.5Ma300 (Fig. 6b) or 5Ma300 (Fig. 8a), may have a positive impact on hydrogen transport. A high density of smaller voids may have a negative impact on the transport of hydrogen through the bulk, since the net residence times in these voids increase due to repeated adsorption/desorption. It is thus difficult to separate explicitly the effects imposed by voids from the effects due to other factors. Transport of hydrogen through the membranes after annealing can be affected by changes in the microstructure—grain growth, strain relief, void formation, composition (segregation), and surface modification (roughening, pitting, nodule growth). Significant grain growth, strain relief, void formation, and roughening were observed in the membranes that exhibited enhanced permeation.

Conclusions

Thermal treatment of thin (1–10 μm), self-supported Pd/Ag membranes developed surface modifications and changes in bulk microstructure. Substantial microstructural changes occurred in the sample regions with high density of grain boundaries, and were, therefore, larger near the substrate/permeate surface than near the growth/feed surface. The changes were associated with surface roughening in all the tested membranes, but with varying magnitude depending on treatment temperature and atmosphere as well as thickness. Voids of varying size developed in the membranes heat treated in air and in the membranes heat treated in N_2/Ar at higher temperatures. Void formation in the air-treated membranes is possibly related to the formation of oxides and stress release associated with volume expansion. In the N_2/Ar-treated membranes, the voids might be initiated by strain relaxation. In addition, some membranes heat treated in air developed nodules at the substrate/permeate surface, which account for an increased surface area of about 10%. In general, the size and density of these defects decline with increasing thickness of the membranes, for both air and N_2/Ar atmospheres. In the thinnest membranes (1.5 μm), some of the voids developed into pits that may severely affect mechanical stability during long-term application and may lead to formation of defects such as pinholes or microcracks.

Effects of N_2/Ar atmosphere on the membranes' microstructure mainly depend on heating temperature. At higher temperatures, significant grain growth and stress relaxation occurred. The temperature range above which enhanced flux was observed is 400–450 °C. This is the temperature range at which remarkable grain growth and other microstructural changes also occurred. In general, the membranes that experienced significant changes in microstructure and surface modification yielded enhanced hydrogen permeation. It is, however, difficult from the microstructural analysis to explain factors related to the reduced permeation for the membranes heat treated in nitrogen and argon below 400 °C.

References

1. Sahaym U, Norton MG (2008) J Mater Sci 43(16):5395. doi:10.1007/s10853-008-2749-0
2. Muradov NZ, Veziroglu TN (2008) Int J Hydrogen Energy 33(23):6804
3. Grashoff GJ, Pilkington CE, Corti CW (1983) Platinum Met Rev 27(4):157
4. McLeod LS, Degertekin FL, Fedorov AG (2007) Appl Phys Lett 90(26):261905-1
5. Ward TL, Dao T (1999) J Membr Sci 153(2):211
6. McCool BA, Lin YS (2001) J Mater Sci 36(13):3221. doi:10.1023/A:1017938403725
7. Yao J, Cahoon JR (1991) Acta Metall Mater 39(1):119
8. Bryden KJ, Ying JY (2002) J Membr Sci 203(1–2):29
9. Yao J, Cahoon JR (1991) Acta Metall Mater 39(1):111

10. Janßen S, Natter H, Hempelmann R, Striffler T, Stuhr U, Wipf H, Hahn H, Cook JC (1997) Nanostruct Mater 9(1–8):579
11. Kirchheim R (1981) Acta Metall 29(5):835
12. Tucho WM (2009) PhD Thesis, Norwegian University of Science and Technology, pp 59–79
13. Okazaki J, Ikeda T, Pacheco Tanaka DA, Suzuki TM, Mizukami F (2009) J Membr Sci 335(1-2):126
14. Xomeritakis G, Lin Y-S (1998) AIChE J 44(1):174
15. Mejdell AL, Klette H, Ramachandran A, Borg A, Bredesen R (2008) J Membr Sci 307(1):96
16. Bredesen R, Klette H (2000) Method of manufacturing thin metal membranes. US Patent 6,086,729
17. ESRF Station Bending Magnet 1B (BM1B) [cited 15-10-2008]
18. Delhez R, de Keijser TH, Langford JI, Louer D, Mittemeijer EJ, Sonneveld EJ (1995) In: Young RA (ed) The Rietveld method. Oxford Univ. Press, Oxford
19. Balzar D, Audebrand N, Daymond MR, Fitch A, Hewat A, Langford JI, Le Bail A, Louer D, Masson O, McCowan CN, Popa NC, Stephens PW, Toby BH (2004) J Appl Crystallogr 37(6):911
20. Larson AC, Dreele RBV (2004) General structure analysis system (GSAS), Los Alamos National Laboratory report 1985–2004. Los Alamos National Laboratory, Los Alamos
21. McCusker LB, Von Dreele RB, Cox DE, Louer D, Scardi P (1999) J Appl Crystallogr 32(1):36
22. Karen P, Woodward PM (1998) J Solid State Chem 141:78
23. Mekonnen W, Arstad B, Klette H, Walmsley JC, Bredesen R, Venvik H, Holmestad R (2008) J Membr Sci 310(1–2):337
24. Brandon DG, Kaplan WD (1999) Microstructural characterization of materials, vol XIII. Wiley, Chichester, p 20
25. Hurlbert RC, Konecny JO (1961) J Chem Phys 34(2):655
26. Dittmeyer R, Höllein V, Daub K (2001) J Mol Catal A: Chem 173(1-2):135
27. Musket RG (1976) J Less Common Metals 45(2):173
28. Elkina IB, Meldon JH (2002) Desalination 147(1-3):445
29. Mejdell AL, Jøndahl M, Peters TA, Bredesen R, Venvik HJ (2009) J Membr Sci 327(1–2):6
30. Thompson CV, Carel R (1995) Mater Sci Eng B 32(3):211
31. Ramachandran A (2009) PhD Thesis, Norwegian University of Science and Technology, pp 51–71
32. Shu J, Bongondo BEW, Grandjean BPA, Adnot A, Kaliaguine S (1993) Surf Sci 291(1-2):129
33. Porter DA, Easterling KE (1991) Phase transformations in metals and alloys. Chapman & Hall, London
34. Gianola DS, Cheng CEXM, Hemker KJ (2008) Adv Mater 20(2):303
35. Koch CC, Scattergood RO, Darling KA, Semones JE (2008) J Mater Sci 43:7264. doi:10.1007/s10853-008-2870-0
36. Uemiya S (1999) Sep Purif Rev 28(1):51
37. Huang M, Wang Y, Chang YA (2004) Thin Solid Films 449(1-2):113
38. Thompson CV (1990) Annu Rev Mater Sci 20:245
39. Rohrer GS (2005) Annu Rev Mater Res 35:99
40. Shugurov AR, Panin AV, Chun H-G, Loginov VA (2005) Science and technology, 2005. KORUS 2005. Proceedings. The 9th Russian-Korean international symposium on
41. Vlasov NM, Fedik II (2002) Int J Hydrogen Energy 27(9):921
42. Vlasov NM, Fedik II (2003) Metal Sci Heat Treat 45(7):328
43. Dutton R (1984) Int J Hydrogen Energy 9(1–2):147
44. O'M Bockris J, Minevski ZS (1998) Int J Hydrogen Energy 23(12):1079
45. Gegner J, Hörz G, Kirchheim R (2009) J Mater Sci 44:2198. doi:10.1007/s10853-008-2923-4
46. Aggarwal S, Monga AP, Perusse SR, Ramesh R, Ballarotto V, Williams ED, Chalamala BR, Wei Y, Reuss RH (2000) Science 287(5461):2235
47. Bucur RV, Ersson NO, Tong XQ (1991) J Less Common Metals 172–174(Part 2):748
48. Gao H, Lin YS, Li Y, Zhang B (2004) Ind Eng Chem Res 43(22):6920
49. Mingmei W, Paul GS (1988) In: Raymond L (ed) Hydrogen embrittlement. ASTM International, Newport Beach